Numerical simulation study on the drag reduction characteristics of grooves-microbubbles coupling surfaces

Tianjian Li[1], Tianlong Yang[1], Qin Dong[1], Xizhi Sun[2,*], Tao Wu[3,*], and Ziqi Xu[3]

[1] School of Mechanical Engineering, University of Shanghai for Science and Technology, Shanghai 200093, China
[2] Department of Mechanical and Aerospace Engineering, Brunel University London, Uxbridge UB8 3PH, UK
[3] R&D Centre, Wuhan Second Ship Design & Research Institute, Wuhan 430205, China

Abstract. Surface drag reduction technologies can significantly reduce the resistance during ship navigation, enhancing speed, efficiency and adaptability under various operating conditions. This paper uses numerical simulation technology to analyze the drag reduction characteristics of grooved and grooves-microbubbles coupling surface, focusing on the effects of groove width, gas flow rate, and liquid flow velocity on the drag reduction performance. The research results indicate that the grooved surface is suitable for full surface drag reduction at velocity below 3 m/s with a maximum drag reduction rate of 4.02%. Microbubbles can greatly improve the drag reduction effect of the grooved surface, and the drag reduction effect of the coupling surface gradually increases with the gas flow rate increases. The maximum drag reduction rate can reach 89.86% at the gas inlet velocity of 1 m/s. The liquid flow velocity has a significant impact on the drag reduction. In both the groove model and the coupling model, the drag reduction rate initially rises and then declines with the liquid flow velocity increases.

Keywords: Grooves / microbubbles / surface drag reduction / numerical simulation

1 Introduction

Ships, as the main means of transportation, play a crucial role in facilitating trade between countries. However, ships require a significant amount of energy during navigation due to the resistance of water. In order to reduce transportation costs, researchers have demonstrated through extensive studies [1–4] that surface drag reduction technologies such as biomimetic grooves and microbubbles can effectively decrease frictional resistance during ship navigation in recent years.

The NASA Langley Research Center in the United States has conducted surface drag reduction tests on grooves since the 1970 s. It was first proposed internationally that arranging small grooves in the downstream direction on the surface can reduce wall friction resistance, breaking the traditional concept that smoother surfaces experience less resistance. Since then, research on surface grooves has been gradually carried out. To describe grooves under different working conditions, Walsh et al. [5] proposed dimensionless parameters $s+$ and $h+$ for groove width s and depth h respectively. It was found that grooves can only have drag reduction effects under working conditions of $h+ \leq 25$ and $s+ \leq 30$ through experimental research. In addition to the size of the grooves, the spacing and shape of the grooves also have a significant impact on the drag reduction rate. Choi et al. [6] and Samuel et al. [7] studied different groove spacings and found that groove spacings produce drag reduction effects by restricting the position of flow vortices. It was tested that reducing the groove spacing can obtain a better drag reduction effect. At present, common groove shapes include triangles grooves, rectangles grooves, semicircles grooves and biomimetic shark skin surfaces. Beckert et al. [8] and Wu et al. [9] conducted simulations and experimental studies on grooved surfaces of different shapes at low liquid flow velocities, and the results showed that rectangular grooves have the highest drag reduction rate. While the comparison of extensive data results has validated the efficacy of groove drag reduction methods, two primary challenges persist in practical applications. Firstly, the optimal groove size varies with sailing speeds [10]. Secondly, the drag reduction effect on the grooved surface is limited, which restricts the widespread application of groove drag reduction methods [11].

In order to achieve more stable and significant drag reduction effects, researchers have begun to explore other surface drag reduction methods, such as microbubble-covered surfaces, superhydrophobic surfaces, oscillating

---

* Corresponding authors: xizhi.sun@brunel.ac.uk;
thewutao@163.com

walls, flexible surfaces and biomimetic structural design [12–16]. Among them, microbubble-covered surface has received widespread attention from researchers. Research has shown that the drag reduction effect of microbubbles is related to the gap between microbubbles, the coverage of microbubbles on the surface and the thickness of the bubble layer. In addition, the movement and distribution of microbubbles are influenced by the diameter, gas flow rate and generation position of microbubbles. The study by Wu et al. [17] demonstrated that the smaller microbubble volumes contribute more favorably to drag reduction. Also, Zhao et al. [18] and Skudarnov et al. [19] indicated that a larger gas flow rate is more favorable for drag reduction at low liquid flow velocities. Gunawan et al. [20] and Gao et al. [21] reported that the better drag reduction effect is achieved when the generation position of bubbles is closer to the front rather than the rear at low liquid flow velocities. Yasunori et al. [22] observed a spontaneous upward motion pattern in their study of microbubble motion behavior. Furthermore, Zhao et al. [23] observed that microbubbles can form an air layer on the surface during liquid flow at increased microbubble flow rates. Montazeri et al. [24] discovered that it starts to disintegrate upon reaching its nominal thickness as the air layer expands, resulting in a ruptured air layer and an associated increase in resistance. However, it should be pointed out that the air layer requires a long distance to develop to the nominal thickness, so the disintegration and rupture of the air layer are generally not considered in simulations or experiments.

After thoroughly comparing existing research outcomes, it becomes evident that there has been sufficient research on the drag reduction effect of ships at lower speeds. However, the analysis of drag reduction under high-speed conditions remains relatively limited. This paper intends to use numerical simulation technology to study the drag reduction characteristics of grooved surfaces and grooves-microbubbles coupling surfaces within the speed range of 0.5–10 m/s, and analyze the effects of groove width, gas flow rate, and liquid flow velocity on the drag reduction rate. Ultimately, the research aims to identify effective drag reduction methods tailored for ships, providing theoretical guidance for enhancing the overall efficiency of ships.

2 Simulation methods

2.1 Governing equations

This paper employs the computational fluid dynamics simulation software Fluent for the simulation and analysis of drag reduction on grooved surfaces and grooves-microbubbles coupling surfaces. The simulation model adopts the Reynolds-averaged Navier-Stokes equation (RANS) based RNG k-ε turbulence model and enhanced wall functions. It uses the SIMPLE algorithm with an iteration residual criterion set at 10^{-6}. In terms of multiphase flow models, according to the study by Zhao et al. [18], it is known that the Eulerian model can better predict microbubble drag reduction compared to the VOF model. Therefore, this paper chooses to use the implicit Eulerian multiphase flow model for the simulations of grooves-microbubbles coupling surfaces.

The governing equations for the k-ε model include the continuity equation, momentum equation, energy equation k and dissipation rate ε. The Reynolds-averaging method is employed to simplify the continuity equation and momentum equation [9].

The continuity equation:

$$\frac{\rho\partial\overline{u_i}}{\partial x_i = 0} \tag{1}$$

where $\overline{u_i}$ is Reynolds average velocity, ρ is fluid density.

The momentum equation:

$$\rho\frac{\partial\overline{u_i}}{\partial t} + \rho\overline{u_j}\frac{\partial\overline{u_i}}{\partial x_j} = -\frac{\partial\overline{p}}{\partial x_i} + \mu\frac{\partial^2\overline{u_i}}{\partial x_i\partial x_j} - \rho\frac{\partial\overline{u_i'u_j'}}{\partial x_j} + \rho\overline{f_i} \tag{2}$$

where, p is pressure, μ is dynamic viscosity, $\overline{u_i'u_j'}$ is Reynolds stress, f_i is mass force.

The energy equation k:

$$\frac{\partial(\rho k)}{\partial t} + \frac{\partial(\rho k\overline{u_i})}{\partial x_i} = \frac{\partial}{\partial x_j}\left[\left(\mu + \frac{\mu_t}{\sigma_k}\right)\frac{\partial k}{\partial x_j}\right] + G_k - \rho\varepsilon. \tag{3}$$

The turbulence kinetic energy dissipation rate ε:

$$\frac{\partial(\rho\varepsilon)}{\partial t} + \frac{\partial(\rho\varepsilon\overline{u_i})}{\partial x_i} = \frac{\partial}{\partial x_j}\left[\left(\mu + \frac{\mu_t}{\sigma_k}\right)\frac{\partial\varepsilon}{\partial x_j}\right] + C_{\varepsilon 1}\frac{\varepsilon}{k}G_k$$
$$- \left(C_{\varepsilon 2} + \frac{C_\mu\eta^3(1 - \eta/\eta_0)}{1 + \beta\eta^3}\right)\rho\frac{\varepsilon^2}{k} \tag{4}$$

when turbulence viscosity $\mu_t = \rho G_\mu\frac{k^2}{\varepsilon}$, turbulence kinetic energy $G_k = \mu_t S^2$,

$$S = \sqrt{2S_{ij}S_{ij}}, \quad S_{ij} = \frac{1}{2}\left(\frac{\partial u_i}{\partial x_j} + \frac{\partial u_j}{\partial x_i}\right), \quad \eta = \frac{Sk}{\varepsilon}.$$

where, $\sigma_k = \sigma_\varepsilon = 1.39, C_{\varepsilon 1} = 1.42$, $C_{\varepsilon 2} = 1.68$, $C_\mu = 0.0845$, $\eta_0 = 4.38$, $\beta = 0.012$.

2.2 Geometric model

Two fluid computational domain models, namely the grooved surface model and the coupling surface model are built to study the drag reduction characteristics on grooved surfaces and grooves-microbubbles coupling surfaces, as shown in Figure 1. The boundary conditions of the model are set as follows: the liquid inlet and gas inlet are velocity inlet, the two sides are symmetrical, the outlet is outflow, and the other surfaces are wall. The key dimensions of the model are length L, width W, and height H. The liquid flows along the length direction (Z direction), and the dimensions of each model are shown in Table 1.

In the Z direction, it is necessary to ensure that the model is sufficiently long due to stress concentration at the inlet affecting the calculation of drag coefficient. The
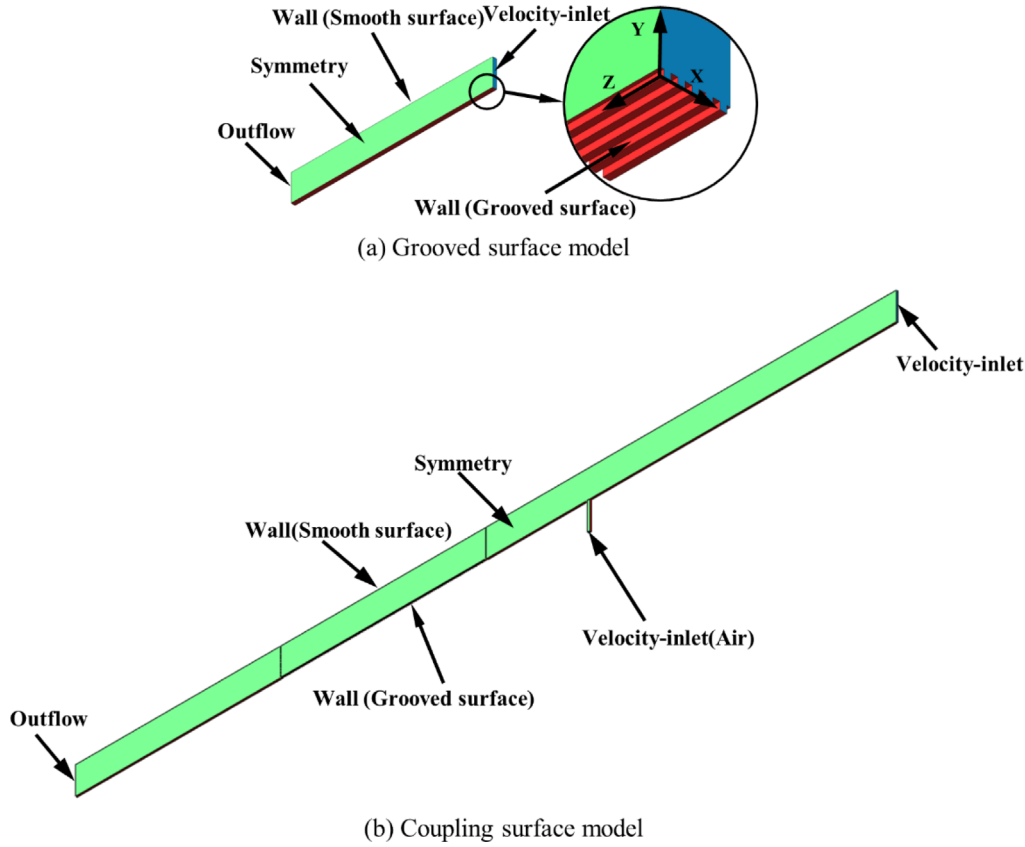
(a) Grooved surface model

(b) Coupling surface model

Fig. 1. Schematic diagram of computational fluid simulation model.

Table 1. Dimensions of computational fluid simulation models.

Figure 1	Grooved surface (model (a))	Coupling surface (model (b))
Length L (mm)	150	600
Width W (mm)	3	1.2
Height H (mm)	20	20

selected groove model length is 150 mm. The coupled model has a more complex structure, and through simulation calculations and testing, a length of 600 mm for the couping model is a reasonable choice that ensures accurate final results and allows for a relatively quick completion of the simulation calculations. In the X direction, the width is determined by the groove width and the groove spacings. Previous research indicates that rectangular grooves have good drag reduction effects [7,25]. Therefore, rectangular grooves are used in this paper. Considering the existing manufacturing capabilities, the groove width is set to be 0.3 mm, and the groove spacing s is set to be 0.6 mm. Also, $h/s = 0.5$ is selected for groove depth resulting in a groove depth h of 0.3 mm [8]. In the vertical Y direction, the upper surface of the model is a smooth surface and the lower surface is a drag reduction surface. The drag reduction rate

is calculated by comparing the drag coefficients of the upper and lower surfaces. The formula for calculating the drag reduction rate is as follows:

$$\eta = \frac{f_{up} - f_{\text{down}}}{f_{up}}, \qquad (5)$$

where f_{up} is smooth surface resistance coefficient, f_{down} is drag reduction surface resistance coefficient.

To avoid interactions between the upper and lower wall surfaces, this paper takes the groove model as an example and conducts preliminary simulations for models of different heights at the liquid flow velocity of 5 m/s. The calculated drag reduction rate results are shown in Table 2. From Table 2, it is evident that the drag reduction rate hardly changes when the height reaches 20 mm. Therefore, this paper sets the height as 20 mm.

Figure 1a is the model of a grooved surface with drag reduction rates calculated for Z values ranging from 50 to 150 mm. Figure 1b represents the model of a grooves-microbubbles coupling surface. In the direction of liquid flow, the gas inlet is positioned 224 mm away from the liquid inlet. The gas inlet has the same width as the model with a length of 2 mm. In the Y direction, the gas inlet is 20 mm away from the grooved surface. The section with $Z=300$–450 mm represents the grooved segment, where the lower surface is the grooved surface, and the remaining wall surfaces are smooth. Drag reduction rates are calculated for Z values ranging from 300 to 450 mm.

Table 2. Calculated drag reduction rate for different model heights.

Model height H (mm)	5	10	20	30
Drag reduction rate η (%)	−6.08	−4.15	−3.73	−3.74

2.3 Model meshing

For the near wall mesh setting, the dimensionless parameter $y+$ is used. It can be expressed as:

$$y^{+} = 0.172 \left(\frac{y}{L} \right) Re^{0.9} \qquad (6)$$

$$Re = \frac{\rho V L}{\mu} \qquad (7)$$

where, y is the height of the first mesh layer, L is the length of the model, ρ is the fluid density, V is the fluid velocity, μ is fluid dynamic viscosity.

The fluid used in the simulation is water, with a density of $\rho = 1000$ kg/m^3, dynamic viscosity $\mu = 1.006 \times 10^{-3}$ kg/(m·s), and the velocity range of the fluid $V_{\mathrm{L}} = 0.5$–10 m/s. The first mesh layer typically requires $y^{+} \leq 1$. Due to the wide range of fluid velocities, the simulation model uses different heights for the first mesh layer to save computational time. When the fluid velocity is less than 5 m/s, the height of the first mesh layer is 0.005 mm (shown as in Fig. 2). When the fluid velocity is greater than or equal to 5 m/s, the height of the first mesh layer is 0.002 mm.

3 Simulation results

3.1 Simulation results of drag reduction on the grooved surface

The main focus of the simulation on the grooved surface is the effect of liquid flow velocity (V_{L}) and groove width on the drag reduction rate (η). During the simulation calculations, the liquid flow velocity is within the range of 0.5 to 10 m/s, with groove widths of 0.25 mm, 0.3 mm and 0.35 mm. The variation curve of drag reduction rates on the grooved surface with different groove widths against the liquid flow velocity is illustrated in Figure 3. As shown in Figure 3, the drag reduction rate shows a trend of first increasing and then decreasing with the increase of liquid flow velocity. When the liquid flow velocity is less than 2 m/s, the smaller the groove width, the greater the drag reduction rate. When the liquid flow velocity is greater than 2 m/s, the larger the groove width, the greater the drag reduction rate. When the liquid flow velocity is 1 m/s and the groove width is 0.25mm, the maximum drag reduction rate on the groove surface appears, with a maximum drag reduction rate of 4.02%. With the increase of the groove width, the range of liquid flow velocities showing a drag reduction effect gradually expands. When the liquid flow velocity is within the range of 1–2 m/s, the

groove surface consistently exhibits a drag reduction effect. However, once the liquid flow velocity exceeds 3 m/s, the groove surface loses its drag reduction effect entirely. This suggests that the grooved surface can only generate a drag reduction effect at relatively low liquid flow velocities.

Figure 4 provides the distribution of wall shear stress on the grooved surface at different liquid flow velocities when the groove width is 0.3 mm. It can be observed that the wall shear stress increases with the increase of liquid flow velocity. Moreover, the stress is mainly concentrated on the upper surface of grooves and at the edges joining the upper surfaces and side surfaces. This result is similar to the computational results reported by Wang et al. [26].

According to the Newton's law of viscosity, shear stress at the fluid-surface contact point can be expressed as follows:

$$\tau = \mu \left(\frac{\partial_u}{\partial_y} \right)_{y=0} \qquad (8)$$

where, μ is fluid viscosity near the groove surface, $(\partial_u / \partial_y)_{y=0}$ is the velocity gradient at the contact between the fluid and the surface.

Surface frictional resistance force can be expressed as follows:

$$F_d = \tau \cdot A_w \qquad (9)$$

where, F_d is the total frictional resistance on the surface, A_w is the wet surface area.

From equations (8) and (9), it can be understood that the frictional resistance experienced by the liquid flowing over the surface is directly proportional to the wall shear stress. Additionally, the wall shear stress is related to the velocity gradient, meaning that the greater the velocity gradient, the larger the wall shear stress. Figure 5 shows the distribution of liquid flow velocity near the grooves at the Z = 100 mm cross-section at different liquid flow velocities. It can be seen that the velocity gradient is larger at the edges joining the upper surface and side surface of the groove. In contrast, the velocity gradient inside the groove is smaller, leading to stress concentration primarily at the edges joining the upper surface and side surface of the grooves. This conclusion is consistent with the research results of Liang et al. [27] and Gu et al. [28]. Figure 5 also reveals that at higher liquid flow velocities, the velocity gradient on the grooved surface is significant, and the grooves struggle to achieve a drag reduction effect. Additionally, the presence of the groove increases the surface contact area with the liquid, leading to a drag reduction rate lower than 0.
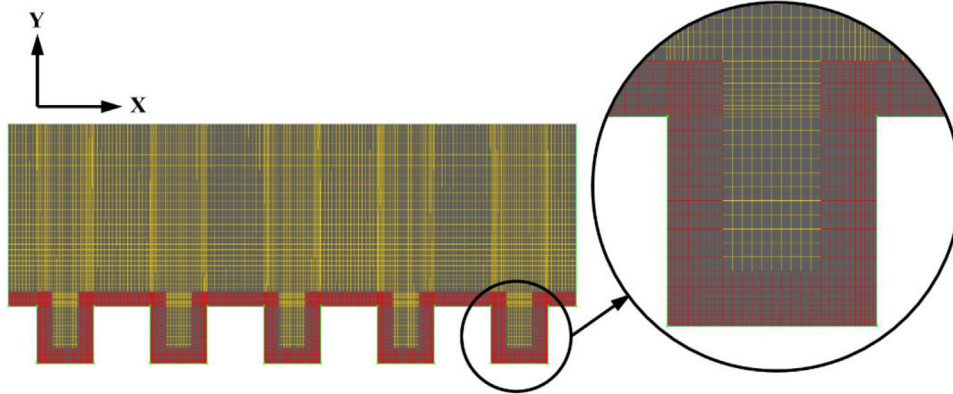
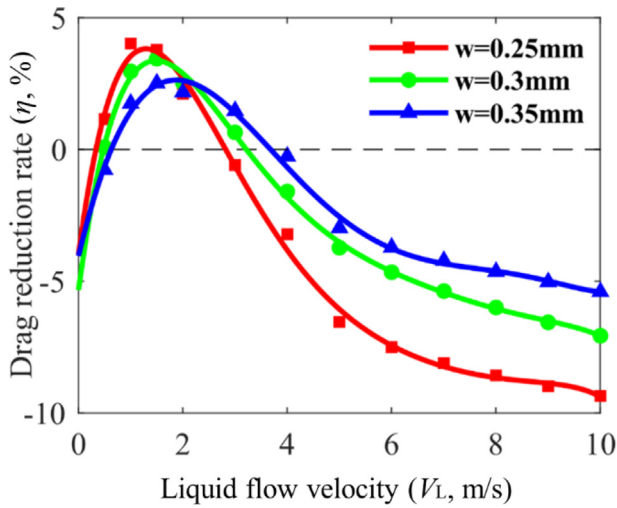**Fig. 2.** Meshing of the grooved surface model ($y = 0.005$ mm).

Fig. 3. Variation curves of drag reduction rate with liquid flow velocity for different groove widths.

3.2 The drag reduction rates of the grooves-microbubbles coupling surface

3.2.1 The effect of gas flow rate on the drag reduction rate of the coupling model

In the coupling model, the groove width is 0.3 mm, and the calculation formula for gas flow rate q is:

$$q = V_G S \rho \tag{10}$$

where, V_G is the gas inlet velocity, S is the gas inlet area, ρ is the gas density.

The gas used in the simulation is air, with a density ρ of 1.225 kg/m^3 and viscosity of 1.7894×10^{-5} kg/(m·s). The gas inlet velocity V_G ranges from 0.1 to 1 m/s, and the gas inlet area S is 2.4 mm^2. The gas flow rates corresponding to different gas inlet velocities are shown in Table 3. The variation curve of drag reduction rate with gas flow rate was obtained through simulation calculation at the liquid flow rate of 5 m/s, as depicted in Figure 6. It can be observed from Figure 6 that the drag reduction rate gradually rises and eventually levels off with an increase of gas flow rate. The drag reduction rate reaches its maximum value of 89.86% at the gas flow rate of 29.40×10^{-7} kg/s. Continuing to increase the inlet velocity to 1.5 m/s, a corresponding gas flow rate of approximately 45×10^{-7} kg/s, the drag reduction rate is 96.35%. It can be observed that when the gas flow rate reaches a certain value, as the gas has almost completely covered the groove surface, further increasing the gas flow rate will only increase the thickness of the gas bubble layer. The drag reduction effect improves slowly, and it becomes unnecessary to further increase the gas flow rate.

The presence of microbubbles transforms the liquid-solid contact into the gas-liquid contact, thereby changing the physical properties of the surface boundary layer. Due to the lower viscosity of gas compared to water, according to equation (8), when the viscosity of the fluid near the wall decreases, the shear stress will decrease, thereby reducing the frictional resistance on the wall and achieving a drag reduction effect. As shown in Figure 7, the gas volume at the bottom of the model increases as the gas flow rate increases, and the fluid viscosity near the grooved surface decreases, thereby increasing the drag reduction rate.

3.2.2 The effect of liquid flow velocity on the drag reduction rate of the coupling models

Based on the results from Section 3.2.1, the drag reduction rate on the microbubble surface has approached 50% with the gas flow rate of 5.88×10^{-7} kg/s. Therefore, the gas flow rate of 5.88×10^{-7} kg/s (corresponding to a gas flow velocity of 0.2 m/s) is selected for simulation calculations at different liquid flow velocities in this section. The liquid flow velocity is maintained within the range of 1–10 m/s. The drag reduction rates on the coupling surface with varying liquid flow velocities are obtained through simulation calculations, as shown in Figure 8. It is observed that with the increase of liquid flow rate, the drag reduction rate initially rises first, then declines and eventually becomes stable. In the simulation calculation results, the maximum drag reduction rate is 60.59% at the liquid flow velocity of 2.5 m/s.

According to the gas distribution shown in Figure 9, it can be observed that microbubbles spontaneously diffuse to the surrounding area as the liquid flows. The diffusion range of microbubbles is inversely proportional to the
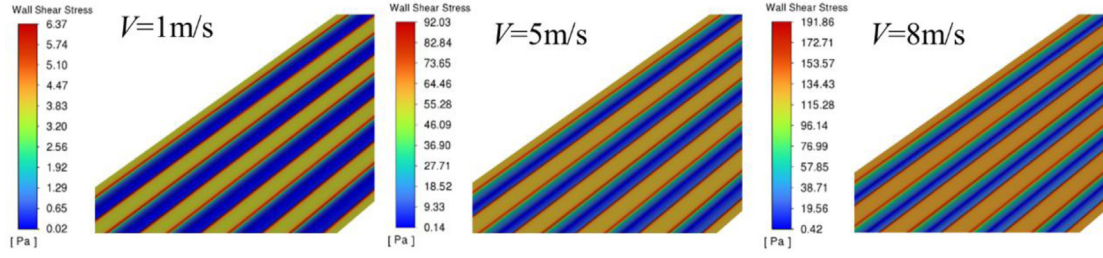
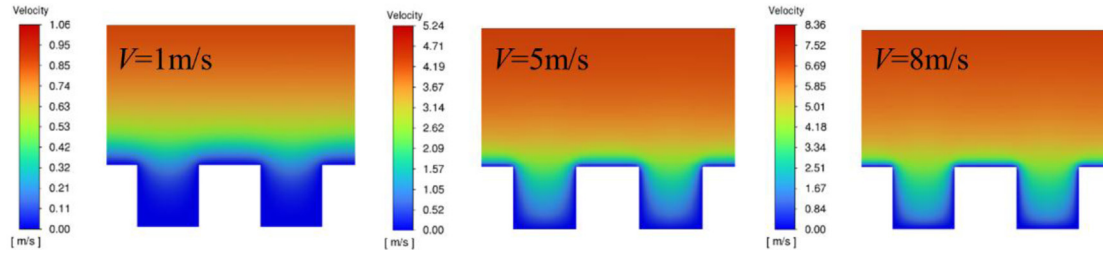**Fig. 4.** Shear stress distribution on the surface wall of the grooves at different liquid flow velocities.

Fig. 5. The gas distribution at $Z = 75$ mm for different liquid flow velocities.

Table 3. Gas flow rates q for different gas inlet velocities V_{G}.

V_{G} (m/s)	0.1	0.2	0.3	0.4	0.5	0.6	0.7	0.8	0.9	1	1.5
q (10^{-7} kg/s)	2.94	5.88	8.82	11.76	14.70	17.64	20.58	23.52	26.46	29.40	44.10
η (%)	28.25	49.31	63.00	69.66	76.71	80.84	83.89	85.43	86.94	89.86	96.35

liquid flow velocity. When the liquid flow velocity is low, the diffusion range of microbubbles is large, and the gas distribution near the groove is uniform.

However, the drag reduction effect of gas not covering the grooved surface is less effective, leading to lower drag reduction rates for the coupling surface model at lower liquid flow velocities. It can be observed that gas accumulates within the groove structure at higher liquid flow velocities. In this scenario, the gas diffusion range is small, resulting in low coverage of gas on the grooved surface. This leads to lower drag reduction rates for the coupling surface model at higher liquid flow velocities.

3.3 Comparative analysis of simulation results

In order to facilitate the comparison of the drag reduction performance of the grooved and grooves-microbubbles coupling surfaces, Table 4 gives the drag reduction rate of these two methods at different liquid flow velocities with a groove width of 0.3 mm. The gas inlet velocity of the coupling surface is 0.2 m/s. According to Table 4, the presence of microbubbles improves the drag reduction effect on the grooved surface. On the other hand, the maximum values of the two drag reduction methods occur at different liquid flow velocities. When the liquid flow velocity is 1m/s, the coupling surface has a lower drag
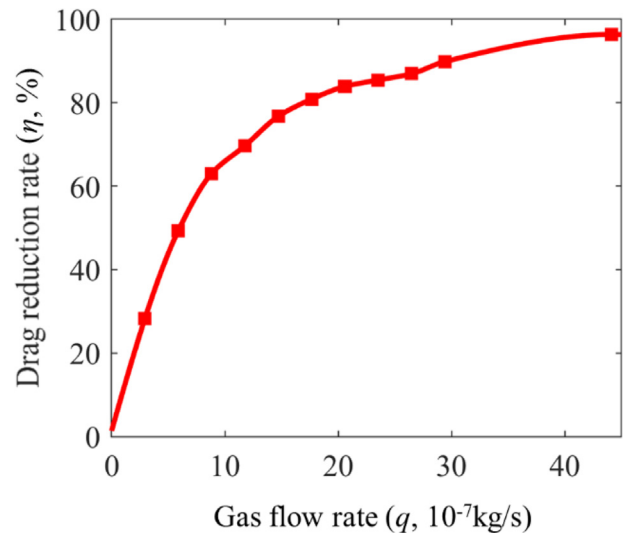

Fig. 6. The variation curve of drag reduction rate with gas flow rate.

reduction rate due to the gas diffusion. Therefore, exploring the drag reduction through the intrinsic structure of the groove is worth considering.
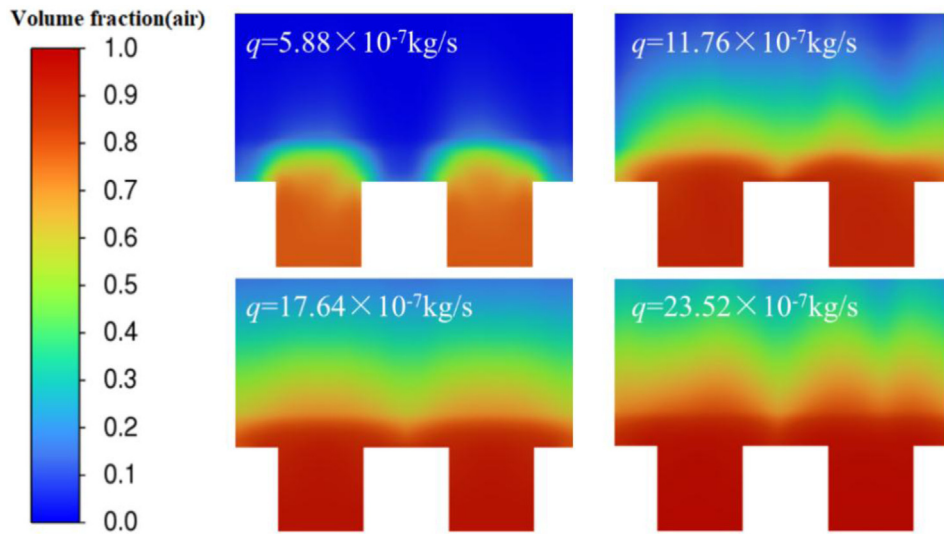
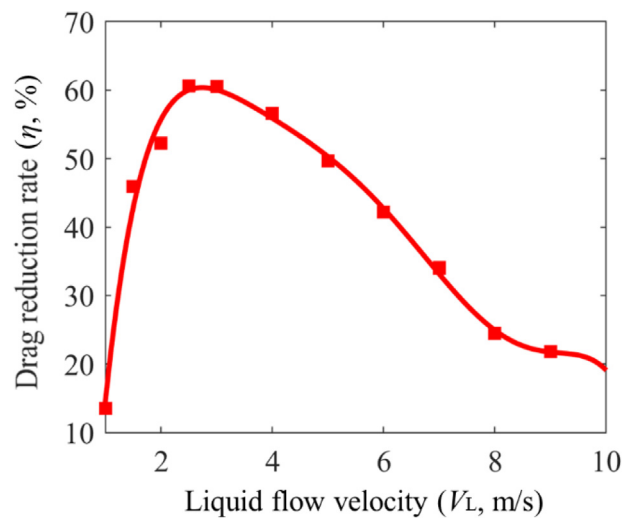**Fig. 7.** The gas distribution at the $Z = 375$ mm for different gas flow rates.

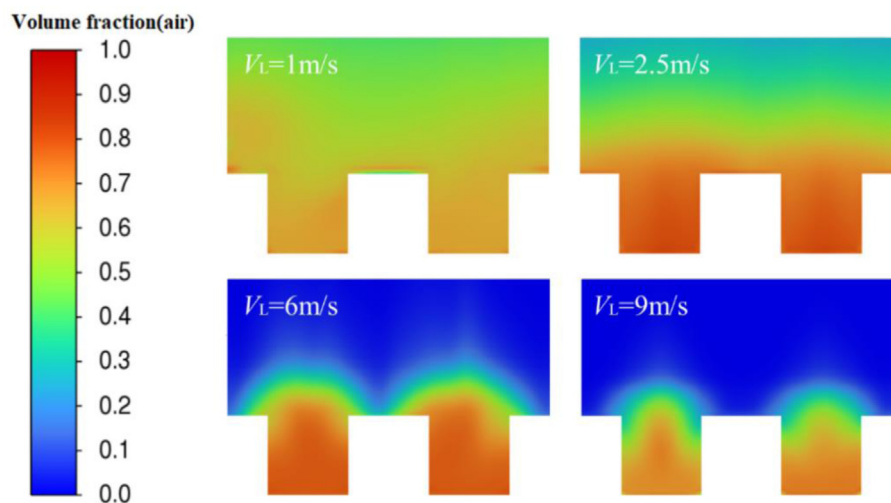**Fig. 8.** The variation curve of drag reduction rate of coupling surface at different liquid flow velocities.

Fig. 9. The gas distribution at $Z = 375$ mm for different liquid flow velocities.

Table 4. Comparison of drag reduction rates for different drag reduction methods at different liquid flow velocities.

Liquid flow velocity	Grooved surface (η_g)	Coupling surface (η_c)	$\eta_c - \eta_g$
1 m/s	2.96%	13.57%	10.61%
1.5 m/s	3.45%	45.91%	42.46%
2 m/s	2.53%	52.21%	49.68%
3 m/s	0.65%	60.50%	59.85%
4 m/s	−1.59%	56.63%	58.22%
5 m/s	−3.73%	49.69%	53.42%
6 m/s	−4.66%	42.17%	46.83%
7 m/s	−5.37%	34.11%	39.48%
8 m/s	−6.00%	24.43%	30.43%
9 m/s	−6.56%	21.83%	28.39%
10 m/s	−7.07%	25.34%	32.41%

4 Conclusions

This paper conducts simulation analyses on the drag reduction effects for the surface of ships with added grooved surfaces and groove-bubble coupling surfaces. In the calculations, liquid flow velocity is employed to represent the ship navigation speed. The study explored the effect of groove width, ship navigation speed and gas flow rate on the drag reduction performance. The research findings are as follows:

– For the grooved surface, the drag reduction rate initially rises and then declines as the liquid flow velocity/ship navigation speed increases. It loses its drag reduction effect when the the liquid flow velocities/ship navigation speed exceeds 3 m/s. The drag reduction rate decreases with increasing groove width at the liquid flow velocities/ship navigation speed below 2 m/s, while the drag reduction rate increases with wider grooves at the liquid flow velocities/ship navigation speed greater than 2 m/s. The range of the liquid flow velocities/ship navigation speed with drag reduction effects expands with increasing groove width. The maximum drag reduction rate reaches 4.02% at the the liquid flow velocity/ship navigation speed of 1 m/s and the groove width of 0.25 mm.

– For the coupling surface, the presence of bubbles greatly increases the drag reduction effect of the grooved surface. The drag reduction rate increases with the increase of gas flow rate, first increases and then decreases with the increase of the liquid flow velocity/ship navigation speed, and finally tends to flatten. The maximum drag reduction rate is 60.59% at the liquid flow velocity of 2.5 m/s. The drag reduction rate of the coupling surface is related to the coverage of microbubbles on the surface. The drag reduction effect can be improved by increasing gas flow rate and finding a suitable the liquid flow velocity/ship navigation speed.

To further enhance drag reduction effects, it is necessary to increase the coverage of microbubbles on the grooved surface. This can be achieved by considering adjustments to the position of the gas inlet or increasing the area of the gas inlet. Exploring suitable methods for gas generation is also crucial in this regard.

References

1. H. Li, J. Yu, Z. Chen et al., Numerical research on drag-reduction characteristics of a body of revolution based on periodic forcing, Ocean Eng. **280** (2023)
2. G. Liu, Z. Yuan, Z. Qiu et al., A brief review of bio-inspired surface technology and application toward underwater drag reduction, Ocean Eng. **199** (2020)
3. M. Soyler, C. Ozalp, C. Polat et al., Experimental and numerical investigation of flow structure of grooved cylinder, Ocean Eng. **264** (2022)
4. J. Zhang, S. Yang, J. Liu, Numerical investigation of frictional drag reduction with an air layer concept on the hull of a ship, J. Hydrodyn. **32**, 591–604 (2020)
5. M. Walsh, A. Lindemann, Optimization and application of riblets for turbulent drag reduction, in 22nd Aerospace Sciences Meeting (American Institute of Aeronautics and Astronautics, 1984)
6. H. Choi, P. Moin, J. Kim, Direct numerical simulation of turbulent flow over riblets, J. Fluid Mech. **255** (1993)
7. S. Martin, B. Bhushan, Modeling and optimization of shark-inspired riblet geometries for low drag applications, J. Colloid Interface Sci. **474**, 206–215 (2016)
8. D.W. Bechert, M. Bruse, W. Hage et al., Experiments on drag-reducing surfaces and their optimization with an adjustable geometry, J. Fluid Mech. **338**, 59–87 (1997)
9. T. Wu, W. Chen, A. Zhao et al., A comprehensive investigation on micro-structured surfaces for underwater drag reduction, Ocean Eng. **218** (2020)
10. J. Wang, Y. Fan, J. Ge et al., The passive control on flow and heat transfer with streamwise micro grooves, Int. Commun. Heat Mass Transfer **135** (2022)

11. S. Kumar, K.M. Pandey, K.K. Sharma, Advances in drag-reduction methods related with boundary layer control – a review, Mater. Today Proc. **45**, 6694–6701 (2021)

12. L. Zhang, X. Shan, T. Xie, Active control for wall drag reduction: methods, mechanisms and performance, IEEE Access **8**, 7039–7057 (2020)

13. D. Kim, H. Lee, W. Yi et al., A bio-inspired device for drag reduction on a three-dimensional model vehicle, Bioinspir. Biomimet. **11** (2016)

14. H.A. Abdulbari, R.M. Yunus, N.H. Abdurahman et al., Going against the flow – a review of non-additive means of drag reduction, J. Ind. Eng. Chem. **19**, 27–36 (2013)

15. M.R. Abbassi, W.J. Baars, N. Hutchins et al., Skin-friction drag reduction in a high-Reynolds-number turbulent boundary layer via real-time control of large-scale structures, Int. J. Heat Fluid Flow **67**, 30–41 (2017)

16. Y. Kametani, K. Fukagata, R. Orlu et al., Effect of uniform blowing/suction in a turbulent boundary layer at moderate Reynolds number, Int. J. Heat Fluid Flow **55**, 132–142 (2015)

17. S.-J. Wu, K. Ouyang, S.-W. Shiah, Robust design of microbubble drag reduction in a channel flow using the Taguchi method, Ocean Eng. **35**, 856-863 (2008)

18. X. Zhao, Z. Zong, Experimental and numerical studies on the air-injection drag reduction of the ship model, Ocean Eng. **251** (2022)

19. P.V. Skudarnov, C.X. Lin, Drag reduction by gas injection into turbulent boundary layer: density ratio effect, Int. J. Heat Fluid Flow **27**, 436–444 (2006)

20. Y. Gunawan, K.T. Waskito, Determination the optimum location for microbubble drag reduction method in self propelled barge model; an experimental approach, Energy Rep. **6**, 774–783 (2020)

21. Q. Gao, J. Lu, G. Zhang et al., Experimental study on bubble drag reduction by the turbulence suppression in bubble flow, Ocean Eng. **272**, (2023)

22. Y. Watanabe, H. Oyaizu, H. Satoh et al., Bubble drag in electrolytically generated microbubble swarms with bubble-vortex interactions, Int. J. Multiphase Flow **136** (2021)

23. X. Zhao, Z. Zong, Y. Jiang et al., A numerical investigation of the mechanism of air-injection drag reduction, Appl. Ocean Res. **94** (2020)

24. M.H. Montazeri, M.M. Alishahi, Investigation of different flow parameters on air layer drag reduction (ALDR) performance using a hybrid stability analysis and numerical solution of the two-phase flow equations, Ocean Eng. **196** (2020)

25. H. Wang, K. Wang, G. Liu, Drag reduction by gas lubrication with bubbles, Ocean Eng. **258** (2022)

26. J. Wang, Y. Fan, J. Ge et al., Effect of streamwise vortex induced[r1] by streamwise grooves on drag reduction and heat transfer performance, Int. J. Thermal Sci. **186** (2023)

27. T. Liang, Y. Xu, J. Li et al., Flow structures and wall parameters on rotating riblet disks and their effects on drag reduction, Alexandria Eng. J. **61**, 2673–2686 (2022)

28. Y. Gu, G. Zhao, J. Zheng et al., Experimental and numerical investigation on drag reduction of non-smooth bionic jet surface, Ocean Eng. **81**, 50–57 (2014)